Icarus 384 (2022) 115109

Contents lists available at ScienceDirect

Icarus

journal homepage: www.elsevier.com/locate/icarus

Research Paper

The roughness of martian topography: A metre-scale fractal analysis of six selected areas

E. Pardo-Igúzquiza [a,*], P.A. Dowd [b]

[a] Instituto Geológico y Minero de España (IGME), Ríos Rosas 23, 28003 Madrid, Spain
[b] Faculty of Engineering, Computer and Mathematical Sciences, The University of Adelaide, Australia

ARTICLE INFO

Keywords:
Local fractal dimension
HiRISE
Metre-scale roughness
Surface texture
Mars

ABSTRACT

Studies of the roughness of natural surfaces (landscapes) provide useful information for planetary geology. This paper covers the mapping and analysis of the spatial variability of the surface roughness of Martian topography at a high spatial resolution (metre-scale). The methodology provides new images of the Martian surface texture at the metre-scale that can assist in the interpretation of geological events, processes and formations. It can also assist in geological mapping and in the evaluation of sites that merit further exploration. Digital elevation models, generated by stereo-pair HiRISE images, of six different terrains (aeolian, volcanic, hydrated, cratered, reticulate and sublimated) were used to characterize the metre-scale terrain roughness of representative test sites on Mars. Surface roughness was evaluated by using the local fractal dimension and the results show that the mean of the local fractal dimension ranges from 2.17 in reticulate terrain to 2.71 in sublimated terrain in the southern polar cap. The roughness of the sublimated terrain is significantly higher than the roughness of typical terrains on Earth. Basically, the roughness of the Martian terrain at the metre-scale depends on the rugosity of the landscape, which can be quantified as the number of metric-scale closed depressions and mounds present on the terrain. The information provided by the spatial variability patterns of metre-scale roughness maps provides a significant resource for local planetary geology research at high resolution scale.

1. Introduction

Landscapes, as described by surface topography, have different degrees of roughness or, alternatively, different degrees of smoothness. Taking a flat surface as a starting point, as the roughness of a landscape increases, so does its complexity, irregularity, and heterogeneity. The evaluation of the landscape roughness of the Earth has received a lot of attention particularly for studying the flow of air (wind) over the ground (Martano, 2000; De Vries et al., 2003), radar scattering (Shepard and Campbell, 1999), ecological habitat studies (Riley et al., 1999; Wilson et al., 2007), characterising geomorphology (Xu et al., 1993; Schwimmer, 2008) and geological studies (Hayes and Kane, 1991) among other applications. A review of roughness in the Earth Sciences can be found in Smith (2014) and a review of the roughness of karst landscapes is given in Day and Chenoweth (2013), and various applications can be found in Glenn et al. (2006), Volker et al. (2007) and Grohmann et al. (2011), among others. Furthermore, on Earth the study of landscape roughness has been extended to the study of the seafloor roughness (Fox and Hayes, 1985), sub-glacial roughness (Cooper et al., 2019) and sea-ice roughness (Segal et al., 2020).

In addition to studies of landscape roughness there are many related studies of the fractal dimension of Earth landscapes (Gilbert, 1989; Huang and Turcotte, 1989) and of planetary geology (Shepard et al., 2001; Sharma and Byrne, 2010; Robbins, 2018). Irrespective of the debates of whether topography is fractal, multifractal or not fractal, in general, topography is rough to some degree. The question is what is an appropriate parameter for characterising topographic roughness? The fractal dimension (FD) of topography is a good candidate. Shepard and Campbell (1999), Shepard et al., 2001) started with the assumption that planetary surfaces are self-affine (fractal) over the scales applicable to radar scattering. Landscape roughness analysis and the mapping of Mars at the global scale using MOLA DEMs (Smith et al., 2001) were considered by Krelavsky and Head (2000), Orosei et al. (2003), Gerekos et al. (2021) and Pardo-Igúzquiza and Dowd (2022), among others. Gerekos et al. (2021) analysed the roughness of 2441 HiRISE tiles using an automated detection of roughness analogues of terrains on Jupiter's moon Europa. However, they do not provide any images of the spatial variability of the roughness or a spatial analysis of the maps. In addition, there is no indication that this analysis has any relevance to the geology of Mars.

* Corresponding author.
E-mail address: e.pardo@igme.es (E. Pardo-Igúzquiza).

https://doi.org/10.1016/j.icarus.2022.115109
Received 13 December 2021; Received in revised form 11 April 2022; Accepted 19 May 2022
Available online 23 May 2022

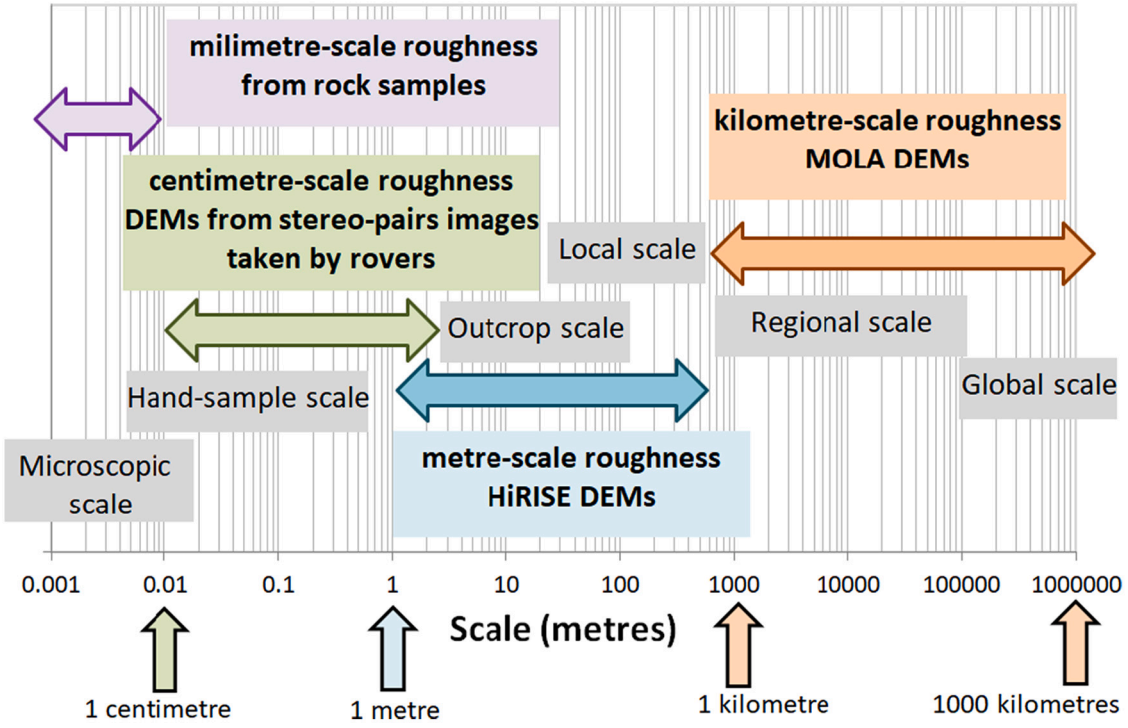

Fig. 1. Martian landscape roughness can be studied at different scales depending on the available experimental data.

The application of landscape roughness maps depends on the scale at which roughness is calculated. In fact, roughness is clearly scale-dependent. The roughness of a surface must be calculated for a specific scale otherwise the results would be meaningless. For example, on Earth one of the smoothest surfaces imaginable in a landscape is a new airport runway (Burrough, 1981), which will have a fractal dimension (smoothness parameter) close to 2 at the metre-scale. However, at the millimetre and micrometre scales (that is, as $h \to 0$) the roughness will be very high because of the irregularities of the aggregate materials of asphalt or concrete which will be very rough at the microscopic scale. Furthermore, the airport runway could be in the middle of the Himalayan Mountains and as such it would be a smooth element in a landscape that is very rough at the kilometre-scale. The same is true of Mars and there are typical ranges of spatial scales at which the topographic roughness of Mars can be investigated using the available data (Fig. 1).

This paper illustrates the mapping and analysis of the spatial variability of the roughness of Martian topography at a high spatial resolution (metre-scale). The local topographic roughness has been assessed by using the local fractal dimension. Histogram, segmentation, connectivity, variability, anisotropy, aggregation, extreme values and shape analysis of the maps of local roughness provide new geomorphometric parameters that can be used by planetary geologists to increase our understanding of the geological and geomorphological processes, products and events that have shaped the landscape of Mars. This analysis is useful because, currently, Martian geology and geomorphology can only be accessed and studied by remote sensing. Any newly acquired information will complement other sources of information and assist planetary geologists in their geological and geomorphological interpretations of the Martian landscape.

The methodology used in this paper to assess the characterization of the spatial variability and structure of local landscape roughness is described in the next section.

2. Methodology

Landscape roughness can be characterized by different mathematical metrics such as the interquartile scale variation (Aharonson et al., 1998, Aharonson et al., 2001), root-mean-square slopes (Krelavsky and Head, 2000), multiscale analysis (Grohmann et al., 2011), wavelets (Deliège et al., 2017), power spectrum density (Liu et al., 2021) and the fractal dimension (Garneau and Plaut, 2000; Pardo-Igúzquiza and Dowd, 2022), among others. The use of the fractal dimension has the appeal of fractal geometry and the fractal character of nature (Mandelbrot, 1983). A fractal is a mathematical set that is irregular or fragmented at all scales and it is a useful model for topography (Burrough, 1981).

The starting point for evaluating landscape roughness is a digital elevation model (DEM) of the area of interest. The DEM is a digital representation of the topography in raster format, that is, the plan projection of the zone of interest is discretised into cells and the topography, or vertical dimension, is represented by assigning an altitude to each cell. A global fractal dimension can be calculated for a DEM but that only gives an average value of roughness for the whole area whereas the interest here is in the spatial variability of topographic roughness obtained by evaluating roughness at the pixel scale of the raster DEM. The methodology used in this paper is to calculate the fractal dimension inside a moving window (Taud and Parrot, 2005) centred at each cell of the DEM, thus assessing the local fractal dimension and, after the application to each cell of the DEM, obtaining a new raster map with the local landscape roughness evaluated for each pixel of the DEM.

The local fractal dimension for each cell (i,j) of the DEM, where the (i) index represents columns and the (j) index represents rows, is calculated by using the intersection of the surface, inside the moving window, with four vertical planes that correspond to the principal geographical directions (N-S, *E*-W, NW-SE and NE-SW). Thus, the problem is reduced to the estimation of the fractal dimension of one-dimensional topographic profiles (Dubuc et al., 1989), inside the two-dimensional moving window of size $\{W+1, W+1\}$.

These topographic profiles are one-dimensional vectors of data. For example, for the (i,j) pixel of the DEM, the E-W profile, which is the (j) row index, is given by:

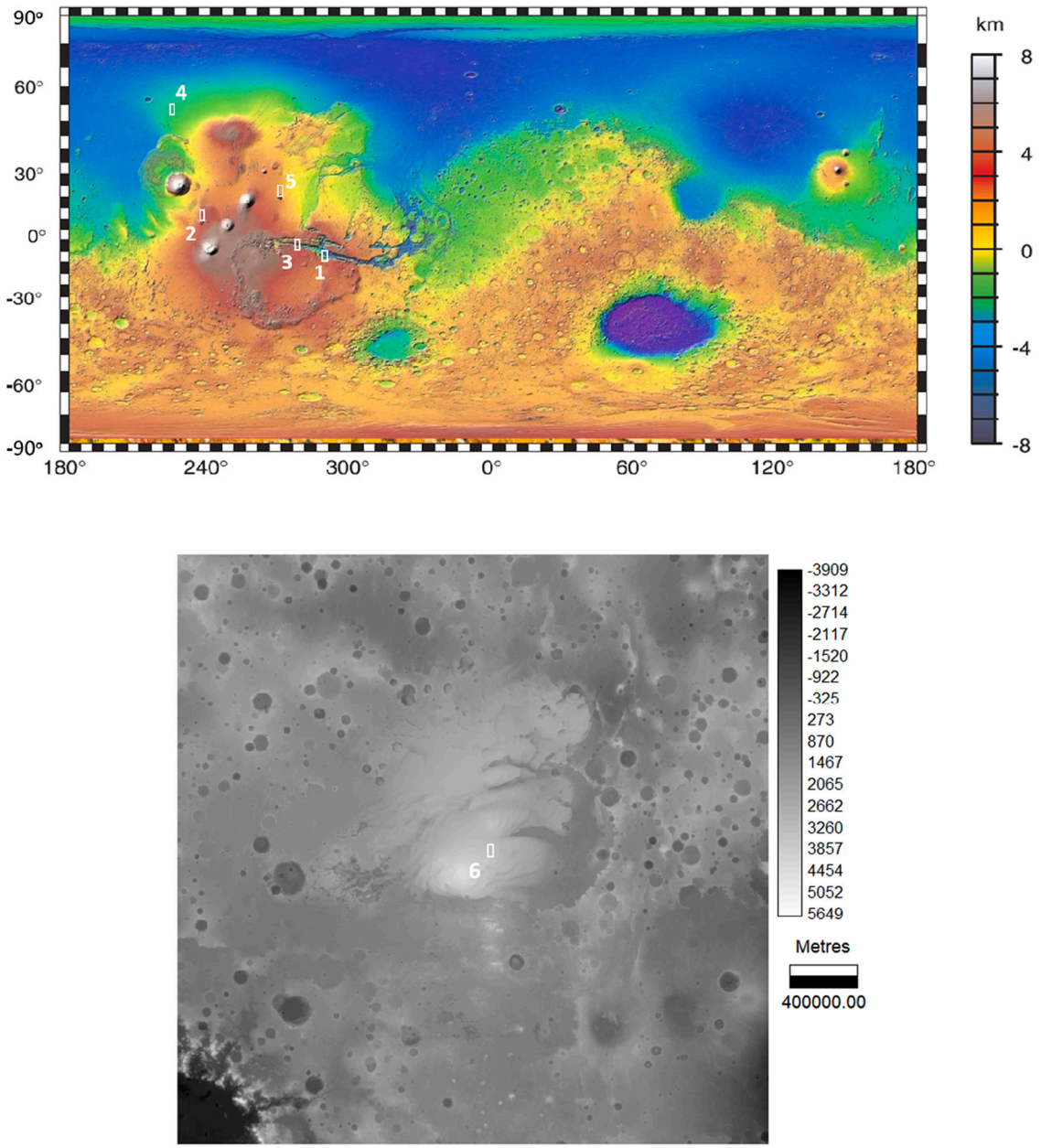

Fig. 2. The white squares show the six test sites used in this paper to study terrain closed depressions and mounds on Martian landscapes: (1) Aeolian terrain in South Melas Chasma, (2) Volcanic terrain in the Tharsis region, (3) Hydrated terrain inside Ius Chasma. (4) Cratered terrain, (5) Reticulate terrain and (6) Sublimated terrain in the layered bands of the Southern polar cap. Mars MGS MOLA Global Colour Shaded Relief from the USGS Astrogeology Science Centre, Goddard Space Flight Centre, NASA and digital elevation model of the Southern Pole.

$$\{z(i-W/2,j),z(i-W/2+1,j),\ldots z(i-1,j),z(i,j),z(i+1,j),\ldots,z(i+W/2-1,j),z(i+W/2,j)\} \quad (1)$$

which is a sequence of $W+1$ values and were $z(i,j)$ is the altitude of pixel (i,j).

Many methods have been proposed for estimating the fractal dimension of one-dimensional vectors of data in time series analysis (Gneiting et al., 2012) and the variogram has proven to be an efficient procedure for doing so (Wen and Sinding-Larsen, 1997; Pardo-Igúzquiza and Dowd, 2020).

The variogram (Matheron, 1963) is a statistical function that estimates the dissimilarity between two random variables separated by a vector of distance h by taking one half of the mean of the squared difference between the two variables:

$$\gamma(h)=\frac{1}{2}\mathrm{E}\{[Z(i+h)-Z(i)]^2\} \quad (2)$$

where $\gamma(h)$ is the variogram for distance h, E{.} is the mathematical expectation operator, and $Z(i)$ is the random variable that describes the altitude at location (i). The motivation for using the variogram method is

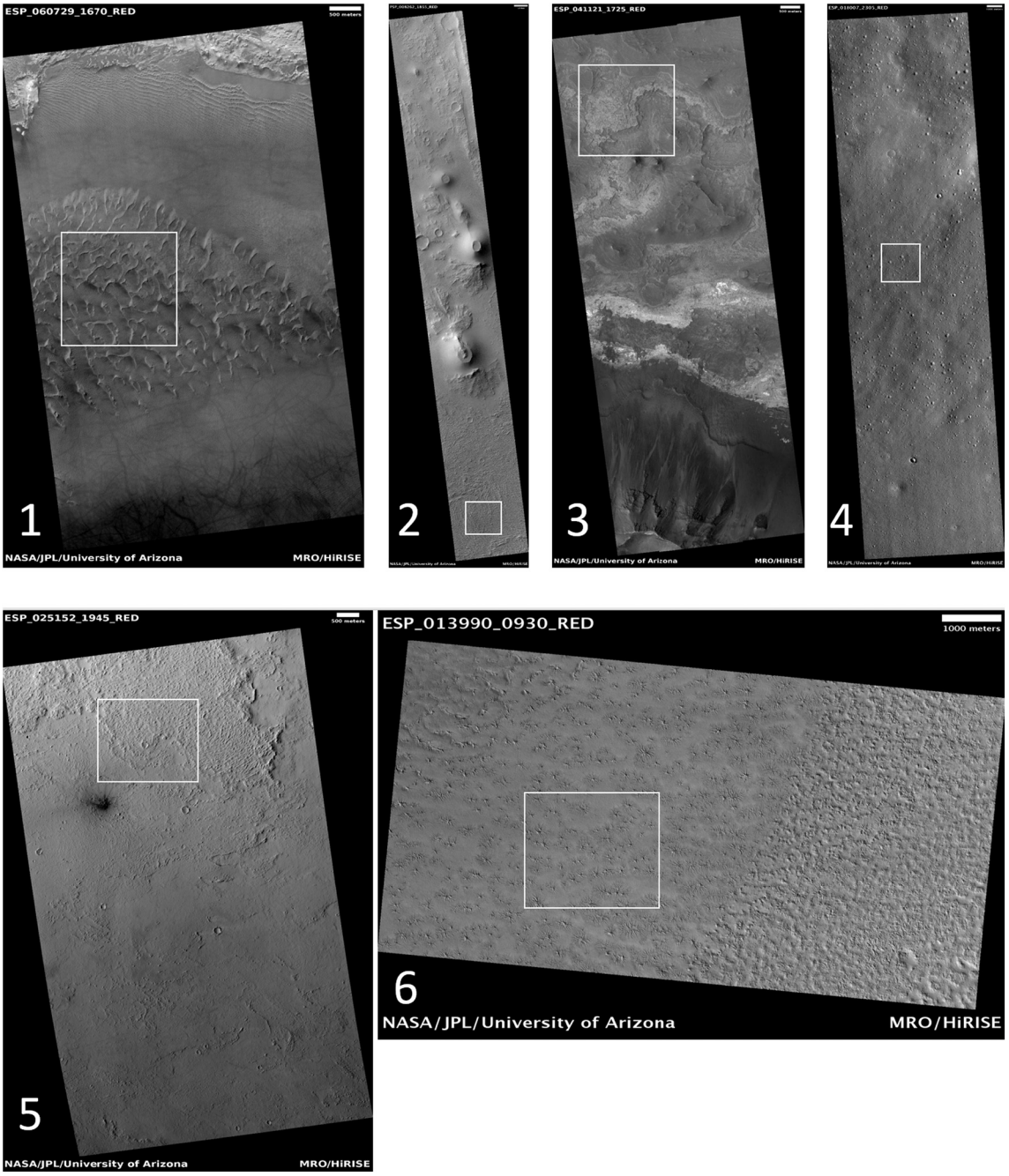

Fig. 3. HiRISE images (1) ESP_060729_1670 for aeolian terrain. (2) PSP_008262_1855 for volcanic terrain. (3) ESP_041121_1725 for hydrated terrain. (4) ESP_018007_2305 for cratered terrain. (5) ESP_025152_1945 for reticulate terrain and (6) ESP_013990_0930 for sublimated terrain.

that fractional Brownian motion (Franceschetti et al., 1999) is a good stochastic model for topographic profiles and natural surfaces and its variogram is a power-law model (Wen and Sinding-Larsen, 1997):

$$\gamma(h) = \alpha h^{\beta}, \tag{3}$$

$$\alpha \geq 0; 0 \leq \beta < 2,$$

where (α, β) are the parameters that define the power variogram model. The use of maximum likelihood to estimate the (α, β) parameters is given in Pardo-Igúzquiza (1998). A method for generating simulations of two-dimensional realisations of random functions using the power variogram model with parameters $(\alpha, 1)$ is described in Pardo-Igúzquiza and Dowd (2003) and a computer code for the inference of parameters is given in Pardo-Igúzquiza (1997).

The 1-D fractal Brownian motion is an appropriate model for a topographical profile, that is, the intersection a topographical surface and a vertical plane (Gneiting and Schlather, 2004). The fractal dimension (FD) is related to the parameter β by the relationship (Voss, 1985):

$$FD = E + 1 - \frac{\beta}{2}, \tag{4}$$

where E is the topological dimension of the Euclidean space of the fractional Brownian motion. For one-dimensional fractional Brownian motion, $E = 1$ and:

$$(FD)_1 = 2 - \frac{\beta}{2}. \tag{5}$$

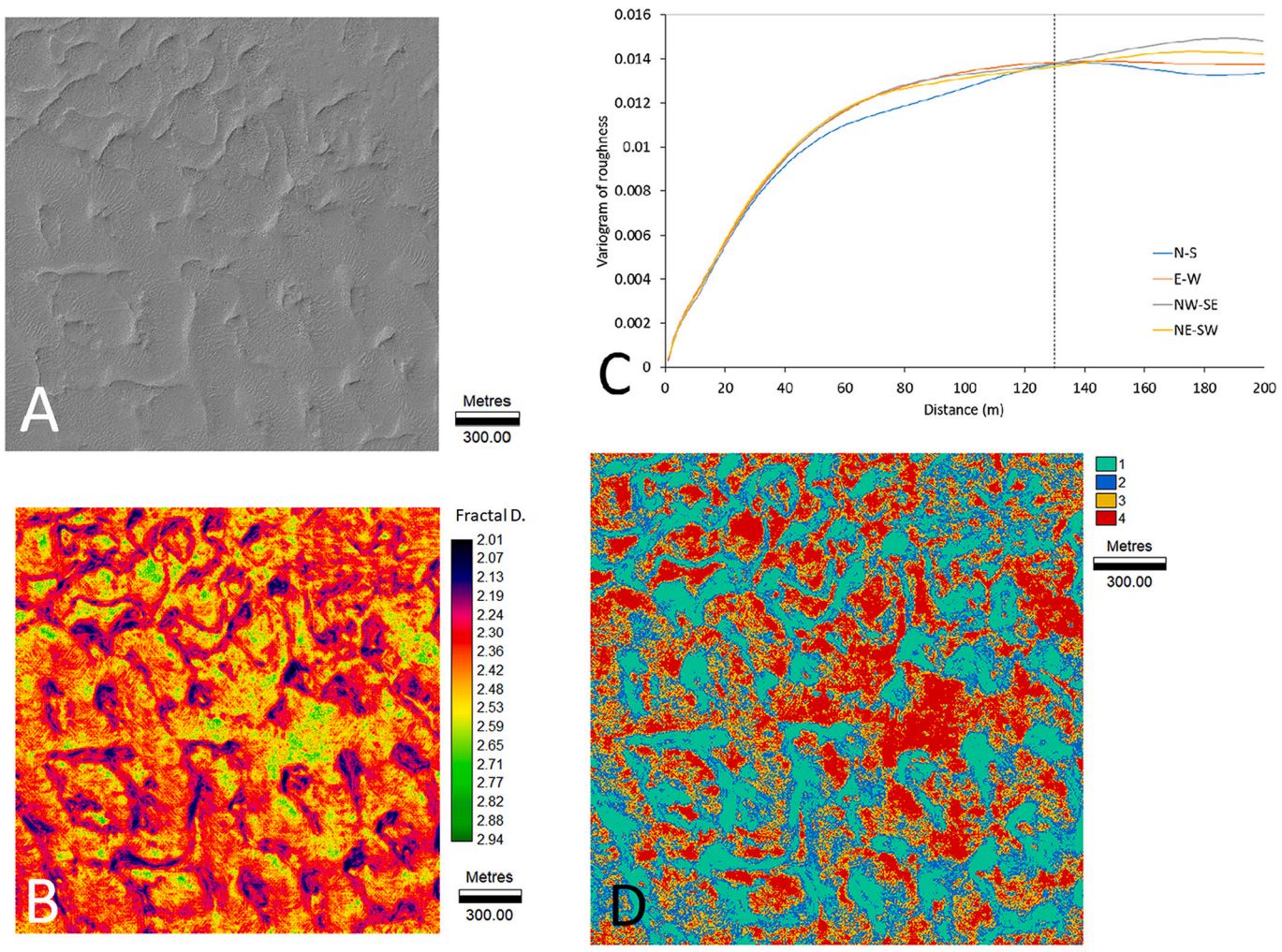

Fig. 4. (A) Hillshade map of the HiRISE digital elevation model of test site 1 (aeolian terrain). (B) Map of roughness defined by the local fractal dimension (Fractal D.). (C) Experimental variogram of (B) for distances up to 200 m. (D) Segmentation of (B) into four classes using the roughness quartiles. Class 1 are values of roughness in the range [2, 2.283), class 2 are values of roughness in the range [2.283, 2.365), class 3 are values of roughness in the range [2.365, 2.445) and class 4 are values of roughness in the range [2.445, 3].

Table 1
Basic statistics of the topographic roughness parameter (fractal dimension FD) for the different types of selected terrain.

Type of terrain	Mean FD	Standard deviation FD	Median FD	10 percentile	90 percentile
Aeolian	2.35	0.118	2.37	2.21	2.52
Volcanic	2.42	0.107	2.42	2.28	2.56
Hydrated	2.26	0.123	2.26	2.14	2.44
Cratered	2.37	0.124	2.37	2.20	2.53
Reticulate	2.17	0.091	2.20	2.11	2.32
Sublimated	2.75	0.089	2.71	2.61	2.80

The fractal dimension of the surface, $(FD)_2$, is estimated from the fractal dimension of the vertical profiles (Voss, 1985):

$$(FD)_2^* = 1 + (FD)_1^*. \tag{6}$$

where the one-dimensional estimated fractal dimension $(FD)_1{}^*$ is obtained from the average of the directional fractal dimensions for the principal geographical directions NS, NE-SW, EW and NW-SE (Pardo-Igúzquiza and Dowd, 2020).

For a profile of length L, the variogram is estimated at K distances or lags $(k; k = 1, \ldots, K)$ where the estimator at the k^{th} lag is given by (Journel and Huijbregts, 1978):

$$\gamma_1(k) = \frac{1}{2(L-k)} \sum_{\ell=1}^{L-k} [z(i) - z(i+\ell)]^2. \tag{7}$$

where $z(i)$ is the observed altitude, which is a realisation of the altitude random variable at the spatial location (i) in the profile given in Eq. (1).

Thus, β can be estimated from the slope of a line fitted to the log-log plot:

$$ln[\gamma_1(k)] = \beta ln[k] + ln[\alpha]. \tag{8}$$

Two reliability parameters, the standard error of the estimated slope parameter (σ_β) and the coefficient of determination (R^2) (Draper and Smith, 1998), can be estimated from the regression equation implied in Eq. (8). The standard error of the slope is used to evaluate the standard error of the estimated fractal dimension while the coefficient of determination provides an assessment of how well the straight-line model in Eq. (8) fits the experimental data. The output from the methodology is a raster map for each of these two reliability parameters and some common values are presented later. The experimental data in Eq. (8) are the estimates of the variogram for K lags which depend on the selected size of the moving window. If the window has a size of $(W + 1) \times (W + 1)$, the variogram is calculated for K lags and the larger the value of W, the more data pairs there will be in Eq. (7) to estimate the variogram. In

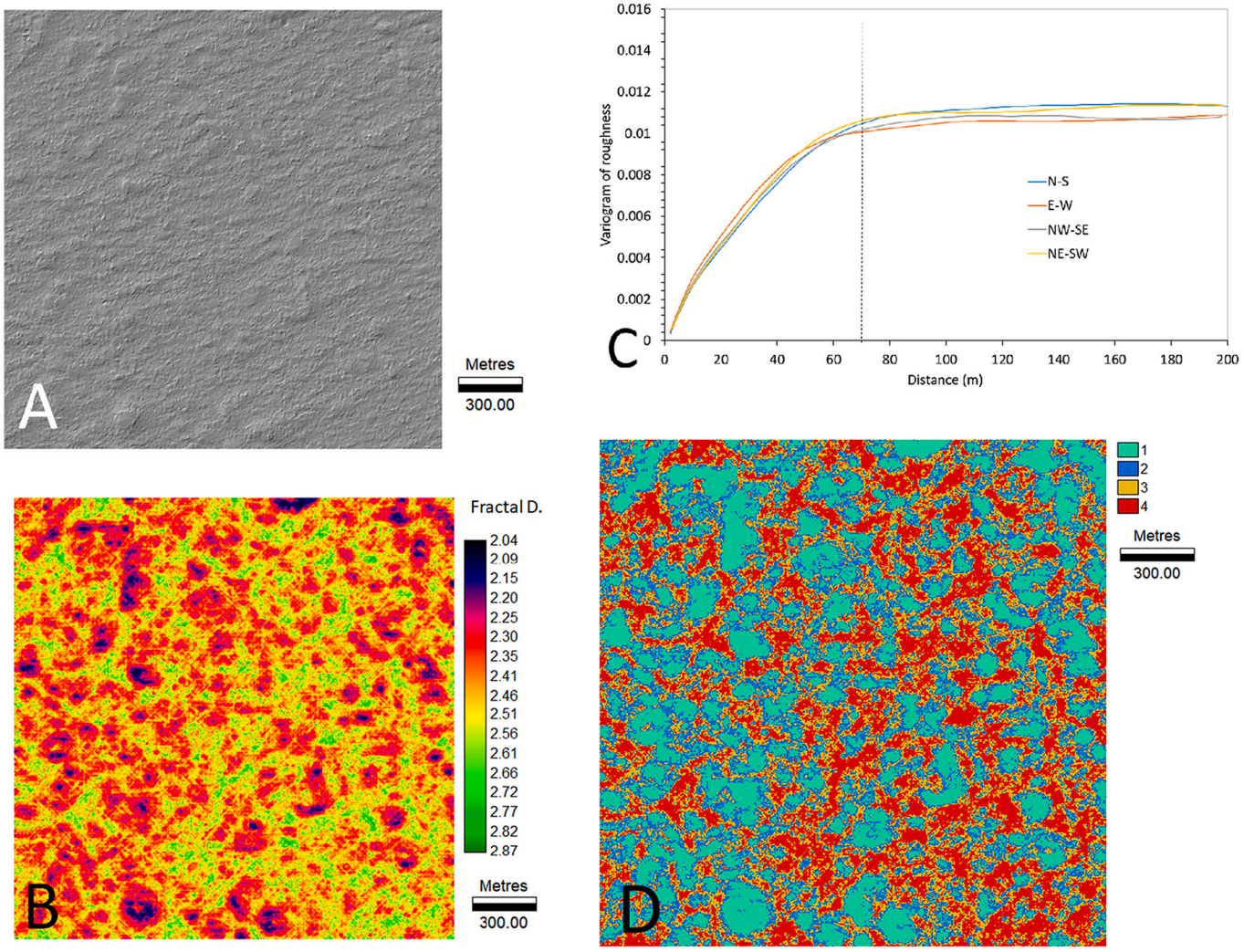

Fig. 5. (A) Hillshade map of the HiRISE digital elevation model of test site 2 (volcanic terrain). (B) Map of roughness defined by the local fractal dimension (Fractal D.). (C) Experimental variogram of (B) for distances up to 200 m. (D) Segmentation of (B) into four classes using the roughness quartiles. Class 1 are values of roughness in the range [2, 2.344), class 2 are values of roughness in the range [2.344, 2.420), class 3 are values of roughness in the range [2.420, 2.493) and class 4 are values of roughness in the range [2.493, 3].

addition, independently of W, the number K of lags will influence the reliability of the estimates (standard error of the slope and coefficient of determination). Pardo-Igúzquiza and Dowd (2020) demonstrates the robustness of the proposed methodology to the size W for a case that is similar to the one used here because the estimated local fractal dimension does not change significantly for variations of the window size of up to 25% of the window considered in this paper (a window size of 41×41 is used in this paper, that is, $W = 40$).

The estimation process generates three raster maps with the same spatial resolution and dimensions as the original DEM. The original DEM is the raster image:

$$\{\mathrm{DEM}(i,j)\,; i = 1,\ldots,NC; j = 1,\ldots,NR\}, \tag{9}$$

where, NC and NR are the number of columns and number of rows, respectively, of the DEM.

The new raster images with the local fractal dimension (FD), standard error of the local fractal dimension (SE) and coefficient of determination (R2) are, respectively:

$$\{\mathrm{FD}(i,j)\,; i = 1,\ldots,NC; j = 1,\ldots,NR\}, \tag{10}$$

$$\{\mathrm{SE}(i,j)\,; i = 1,\ldots,NC; j = 1,\ldots,NR\} \tag{11}$$

and

$$\{\mathrm{R2}(i,j)\,; i = 1,\ldots,NC; j = 1,\ldots,NR\}, \tag{12}$$

The layer of the local fractal dimension, representing local roughness, can be spatially analysed and new geomorphometric parameters can be calculated by analysing the histogram, segmentation, variability, anisotropy, aggregation, connectivity, extreme values, and shape analysis.

The histogram of the local roughness map is an estimate of the probability density function of the variable and describes the frequency of values of the local fractal dimension in the interval between 2 and 3. The shape of the histogram, its mode and other statistics may be specific to individual terrains. These and other statistics described below can be calculated for the entire zone or for different areas.

The local roughness image can be segmented by applying a set of local fractal dimension thresholds to generate a new raster image of the spatial disposition of zones of, for example, very high, high, medium, low, and very low roughness, for which four thresholds are required. Segmentation is essentially a reclassification of the local fractal dimension image to highlight areas of different roughness values. If only one threshold is applied, the result is a binary image with only two values representing areas of roughness above or below the threshold.

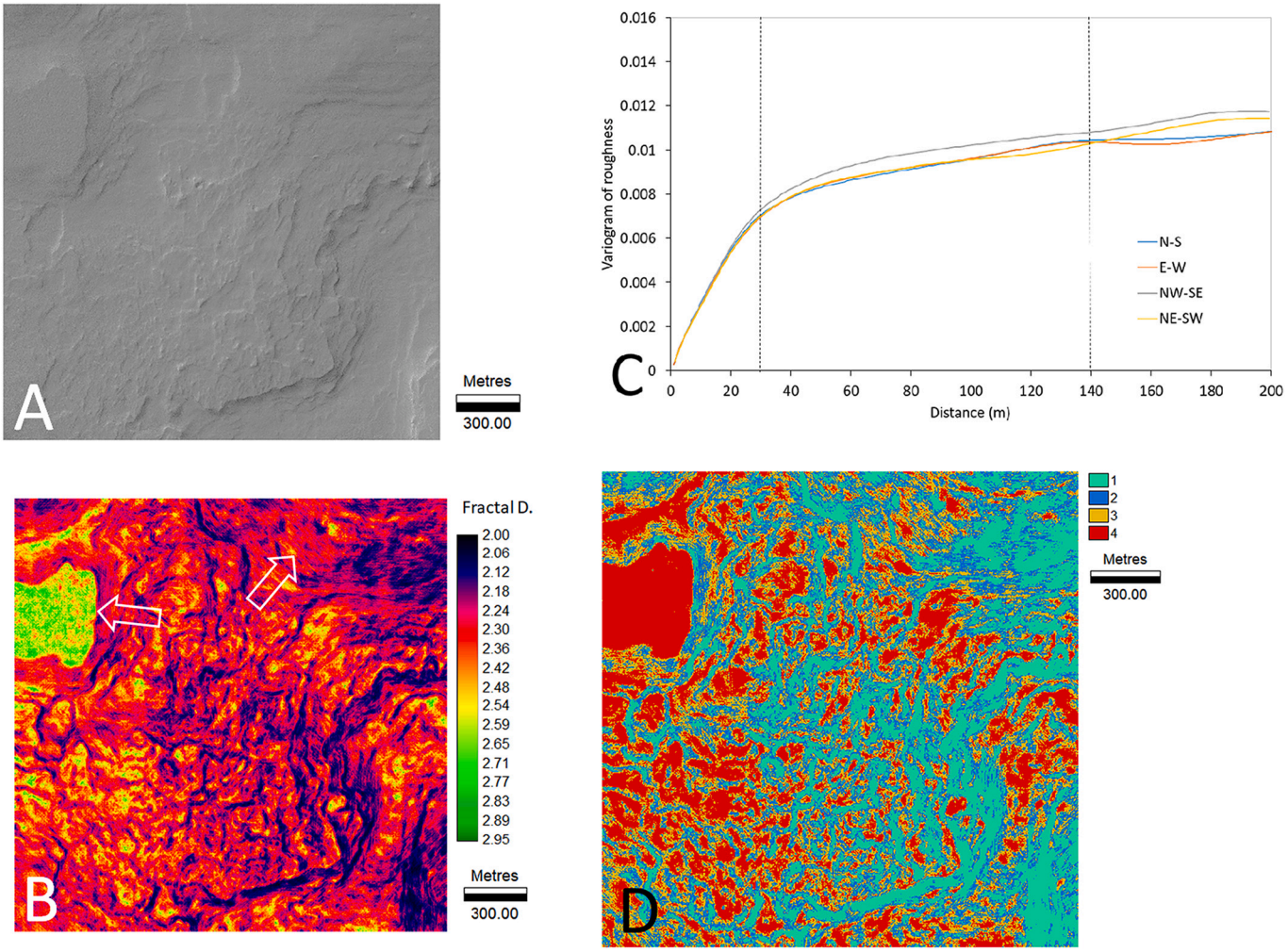

Fig. 6. (A) Hillshade map of the HiRISE digital elevation model of test site 3 (hydrated terrain). (B) Map of roughness defined by the local fractal dimension (Fractal D.). (C) Experimental variogram of (B) for distances up to 200 m. (D) Segmentation of (B) into four classes using the roughness quartiles. Class 1 are values of roughness in the range [2, 2.192), class 2 are values of roughness in the range [2.192, 2.259), class 3 are values of roughness in the range [2.259, 2.342) and class 4 are values of roughness in the range [2.342, 3].

The variability or spatial continuity can be estimated by applying the variogram in Eq. (7) to the image of local roughness given in Eq. (10). The shape and parameters of the variogram can be used to characterize the spatial variability of roughness in a particular zone. Anisotropy can be evaluated by calculating the variogram of the local roughness image for different geographical directions. Aggregation and connectivity can also be characterized by the variogram estimated from a binary variable provided by segmentation. These represent the degree of fragmentation of a given interval of the values of local roughness. For example, if a fractal dimension threshold is chosen to define very high roughness (i.e., extreme values), the aggregation and connectivity of these extreme values can be estimated by calculating the variogram of the binary image. Finally, shape analysis can be used to detect particular shapes of roughness such as lineations, abrupt changes, and round shapes.

The previous list of geomorphometric parameters covers the main parameters for characterising the spatial variability of local roughness but it could be expanded if necessary. The geomorphometric parameters could be applied to DEMs of Earth terrains, mainly in arid areas, to provide standards for comparison. However, that is outside the scope of this paper.

3. Case study

The digital elevation models (DEMs) used in this paper are the most accurate local topographic maps available for Mars and were obtained from images gathered by the High Resolution Imaging Science Experiment (HiRISE) cameras (McEwen et al., 2010) on board the NASA Mars Reconnaissance Orbiter spacecraft (Graf et al., 2005) and were downloaded from the HiRISE internet site (https://www.uahirise.org/dtm/). HiRISE images are contributing significantly to our knowledge of Martian geology at the local scale. The DEMs are derived from high-resolution stereo-pair images (Kim et al., 2013) and they have an altimetric uncertainty of a few tens of centimetres (McEwen et al., 2010) and a spatial resolution between 1 and 2 m.

Six HiRISE derived DEMs were selected for this study and their spatial locations are shown in Fig. 2. The six HiRISE images are shown in Fig. 3 and the test sites selected for each HiRISE DEM are shown as white squares in Fig. 3. The DEM for each test site represents a surface of 2 km $\times$ 2 km in terrain units, and each comprises a raster image of 2000 rows and 2000 columns for the 1 m resolution DEMs and raster images of 1000 rows and 1000 columns for the 2 m resolution DEMs. The shaded relief, or hillshade maps, (Marston and Jenny, 2015) from the DEMs of the test sites are shown in Figs. 4A–9A for aeolian terrain (AT), volcanic terrain (VC), hydrated terrain (HT), cratered terrain (CT), reticulate terrain (RT) and sublimated terrain (ST), respectively. The six terrains are named after the most distinctive, but not unique, morphological process that shaped the examined landscape. This is considered to be a representative, but not exhaustive, selection of Martian landscapes for

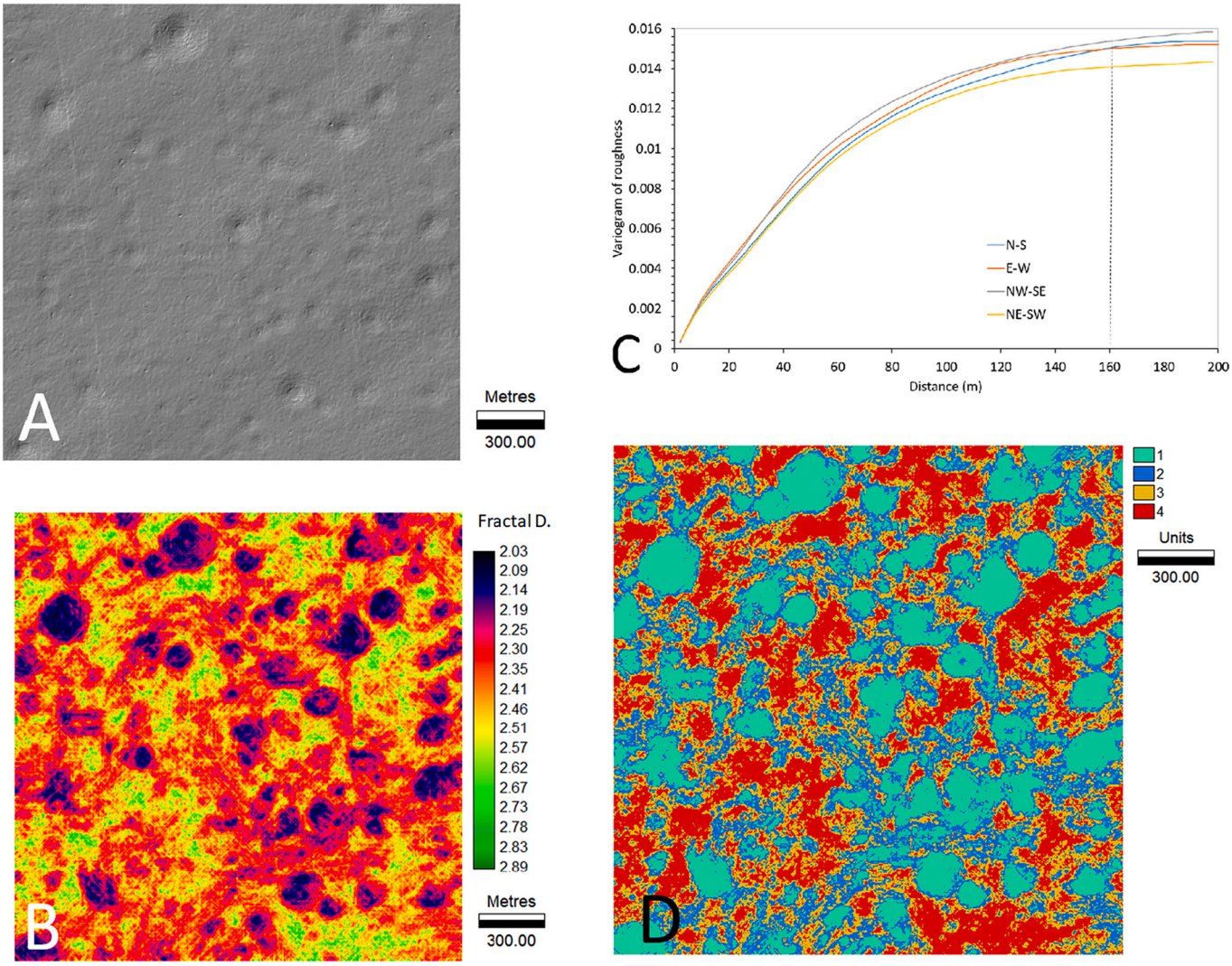

Fig. 7. (A) Hillshade map of the HiRISE digital elevation model of test site 4 (cratered terrain). (B) Map of roughness defined by the local fractal dimension (Fractal D.). (C) Experimental variogram of (B) for distances up to 200 m. (D) Segmentation of (B) into four classes using the roughness quartiles. Class 1 are values of roughness in the range [2, 2.278), class 2 are values of roughness in the range [2.278, 2.366), class 3 are values of roughness in the range [2.366, 2.452) and class 4 are values of roughness in the range [2.452, 3].

roughness mapping and for analysing the landscape at the metric-scale. The selection of the sites was arbitrary although the intention was to use a wide variety of different origins of the Martian landscapes. The procedure can be applied to any DEM for any part of Mars. Test site 1 (Fig. 2) in the southern part of the Melas Chasma in Valles Marineris was selected as representative of aeolian terrain (AT), that is, with a landscape sculpted by the wind. Test site 2 (Fig. 2) in the northern part of Ulysses Tholus and close to Ulysses Fossae in the Tharsis dome was selected as being representative of volcanic terrain (VT), that is, with a landscape sculpted by volcanic processes. Test site 3 (Fig. 2) inside Ius Chasma in Valles Marineris was selected as representative of hydrated terrain (HT), a light-toned landscape representative of diapiric-like processes. Test site 4 (Fig. 2) in Lycus Sulci northwest of Olympus Mons was selected as representative of cratered terrain (CT), that is, a landscape representative of impact cratering without any resurfacing by other processes. Test site 5 (Fig. 2), on the northern flank of the Tharsis Tholus volcano, was selected as being representative of reticulate terrains (RT), that is, a landscape representative of polygenetic processes. Test site 6 (Fig. 2) in the Southern Polar cap was selected as representative of sublimated terrain (ST), that is, a landscape representative of a CO_2 ice sublimation process. These six text sites are the same as those used in Pardo-Igúzquiza and Dowd (2022) for the mapping and spatial analysis of closed depressions and mounds.

The methodology for mapping roughness using the local fractal dimension, as estimated by using the variogram, was applied to the six test sites described above. The graphical results are shown in Figs. 4B–9B for aeolian, volcanic, hydrated, cratered, reticulate and sublimated terrains respectively. Typical maps of the standard error of the estimated fractal dimension and the coefficient of determination are shown in Fig. 10 for the aeolian terrain. The mean of the standard error (standard deviation of the estimation variance) of the estimated local fractal dimension is 0.079, the 90 percentile is 0.096 and the maximum is 0.120. Thus, for 90% of the area in Fig. 10A, the standard error is less than 0.096. With respect to the coefficient of determination in Fig. 10B, the mean is 0.959 and the 10 percentile is 0.854 meaning that 90% of the area in Fig. 10B has a coefficient of determination greater than 0.854.

The histograms of the fractal dimension for all areas of the test sites are shown in Fig. 11A and the main statistics of these histograms are shown in Table 1. The figures and the table show that the sublimated terrain, with a mean fractal dimension of 2.71, is the landscape with the highest local roughness. They also show that the volcanic terrain, with a mean fractal dimension of 2.42, is the terrain with the second highest local roughness. The terrain with the smoothest landscape, with a mean fractal dimension of 2.20, is the reticulate terrain followed by the

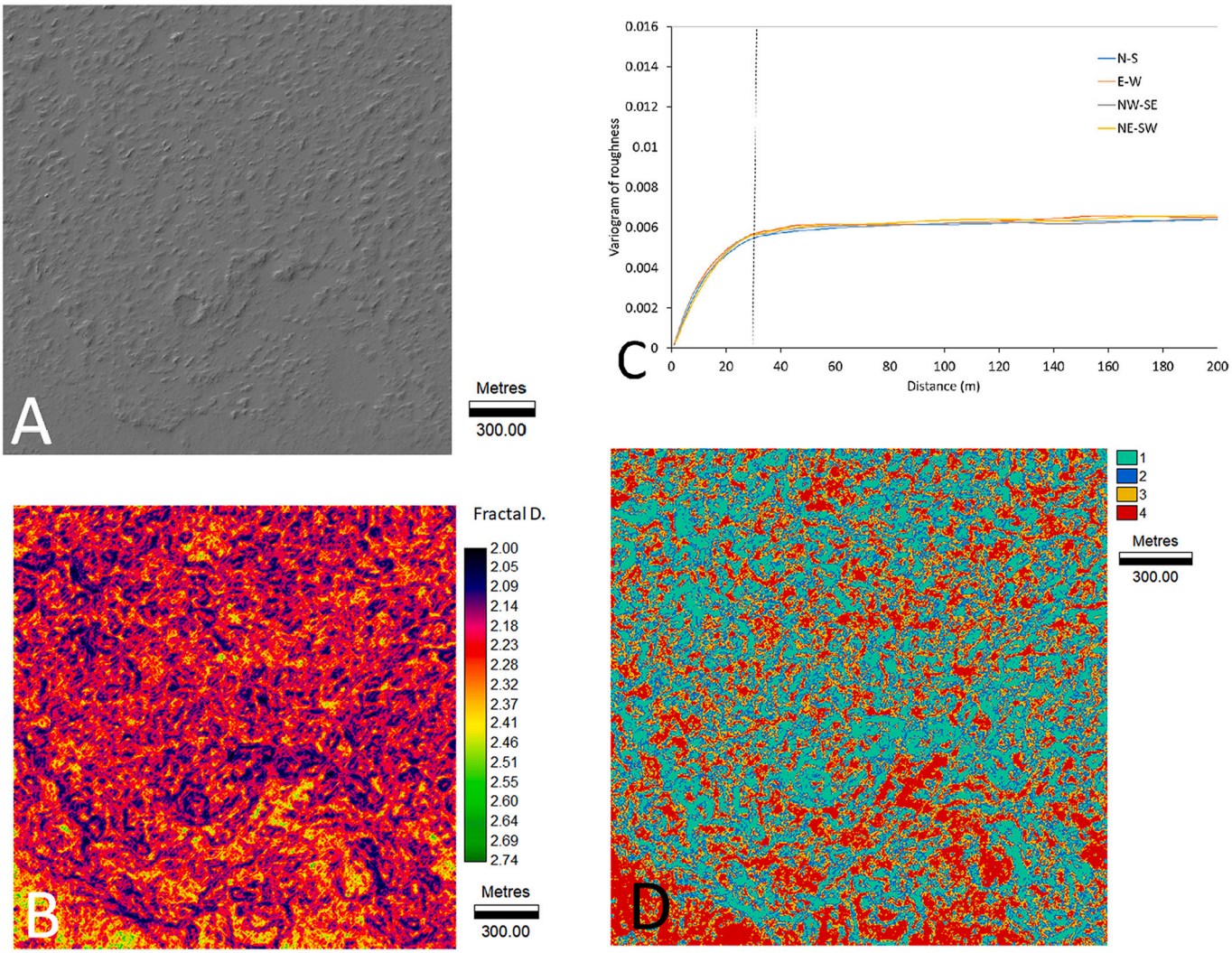

Fig. 8. (A) Hillshade map of the HiRISE digital elevation model of test site 5 (reticulate terrain). (B) Map of roughness defined by the local fractal dimension (Fractal D.). (C) Experimental variogram of (B) for distances up to 200 m. (D) Segmentation of (B) into four classes using the roughness quartiles. Class 1 are values of roughness in the range [2, 2.144), class 2 are values of roughness in the range [2.144, 2.195), class 3 are values of roughness in the range [2.195, 2.257) and class 4 are values of roughness in the range [2.257, 3].

hydrated terrain with a mean local fractal dimension of 2.26. Finally, the aeolian and cratered terrains have medium roughness each with a mean local fractal dimension of 2.37. Notwithstanding this ranking of the terrain by mean local fractal dimension, there is significant variation in the local fractal dimension for each terrain as can be seen in the roughness maps in Figs. 4B–9B and the histograms in Fig. 10A. Thus, if for each terrain the 10% of the highest and the 10% of the lowest fractal dimensions are not considered, 80% of the fractal dimensions are included in the 10 to 90 interval percentiles which are (2.21, 2.52, 2.28, 2.56, 2.14, 2.44, 2.20, 2.53, 2.11, 2.32, 2.61, 2.80) for the aeolian, volcanic, hydrated, cratered, reticulate and sublimated terrains respectively. In addition, the local fractal dimension is spatially structured in ridges of low roughness values and patches of high roughness values. Furthermore, in addition to showing the spatial variability of landscape roughness, the local fractal dimension maps may reveal some spatial patterns that are hidden in the landscape as shown by the white arrows in Fig. 6B for the hydrated terrain and Fig. 9B for the sublimated terrain. In the hydrated terrain the white arrow at the right points to a fine orientation in the roughness due to a plastic flow of material while the white arrow on the left points to a marked contrast between high and low values of roughness that delineate a structure that merits further attention. In the sublimated terrain the two white arrows point to linear structures that could be artefacts generated in the DEM processing.

Fig. 12 shows six typical topographic profiles, each 500 m in length, one for each terrain type. The mean local fractal dimension is similar to the mean fractal dimension for the corresponding type of terrain as given in Table 1. These profiles illustrate the landscape roughness as seen in topographic profiles.

4. Discussion

The fractal dimension used in this paper is related to the Hurst parameter H that characterises long memory processes (Beran, 1994), considering that $\beta = 2H$ (Voss, 1985). Thus, the fractal dimension used here could be called the Hurst fractal dimension (HFD) in order to distinguish it from other fractal dimensions. For example, strictly defined, the term fractal refers to a set in which the Hausdorff–Besicovitch dimension exceeds the topological dimension (Mandelbrot, 1977). For a linear fractal function, the Hausdorff dimension D may vary between 1 (completely differentiable) and 2 (so rough and irregular that it effectively takes up the whole of a two-dimensional topological space) (Burrough, 1981). That is the case for a random walk that wanders over a square and fills the space as seen in Fig. 13A. However, the latter is not possible for a random walk that represents a

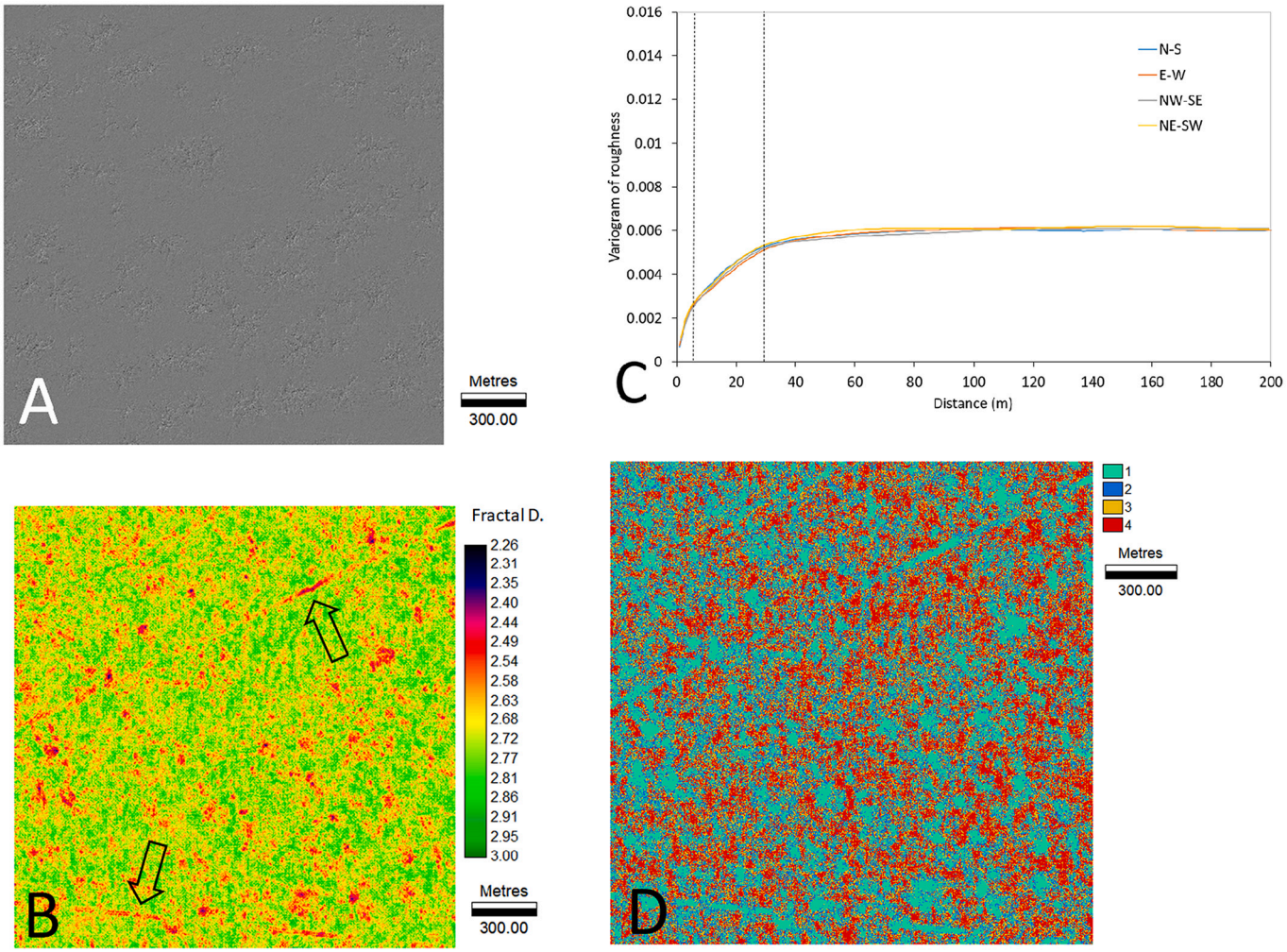

Fig. 9. (A) Hillshade map of the HiRISE digital elevation model of test site 6 (sublimated terrain). (B) Map of roughness defined by the local fractal dimension (Fractal D.). (C) Experimental variogram of (B) for distances up to 200 m. (D) Segmentation of (B) into four classes using the roughness quartiles. Class 1 are values of roughness in the range [2, 2.659), class 2 are values of roughness in the range [2.659, 2.713), class 3 are values of roughness in the range [2.713, 2.762) and class 4 are values of roughness in the range [2.762, 3].

topographic profile (Fig. 13B) or a time series because both are ordered sequences of data where there is a unique value of the variable (altitude) for each space or time coordinate. Furthermore, for a topographic profile the maximum roughness is achieved by a white noise that has a HFD of 2 (and 3 for a surface). However, its Hausdorf–Besicovitch FD is 1.5 for a profile and 2.5 for a surface.

The local fractal dimension treats the fractal dimension as a spatially variable parameter. From these maps, shown in this paper in Figs. 4B–9B, the concept of fractally homogeneous regions (Klinkenberg, 1992) could be applied. This is a straightforward procedure using the reclassification of raster maps and a Geographical Information System. The only problem is the selection of the thresholds of fractal dimensions that define the homogeneous regions according to a geomorphological or geological task.

The local fractal dimension, i.e., the roughness of the terrain, could be related to the number of closed depressions that are found on each terrain. In this sense Fig. 14 shows the relationship between the mean local fractal dimension of each of the terrains and their number of closed depressions. The number of closed depressions is covered in Pardo-Igúzquiza and Dowd (2022). From Fig. 14 it appears that low fractal dimensions correspond to small numbers of closed depressions and high numbers of closed depressions correspond to high fractal dimensions or high roughness of the terrain. The correspondence between the two extremes is not perfectly linear.

To provide a reference for comparison, the local fractal dimension has been calculated for some Earth DEMs with spatial resolutions equal to those of the Martian HiRISE DEMs. Although there are millions of examples that could be used, only six cases have been considered and these include two volcanic terrains, two karst terrains and two aeolian terrains. For the aeolian terrains, one is a natural aeolian terrain and the other is the same terrain plus an adjacent anthropic terrain. The areas of these test sites are identical to the areas of the Martian test sites and the histograms of the estimated local dimensions are given in Fig. 11B. In general, the local Earth fractal dimensions are less than the Martian local fractal dimensions although they may be similar. It is difficult to find on Earth the level of roughness of the Martian sublimated terrain although we have tried a minimal sample in the huge number of DEMs that could be analysed for Earth terrains.

The following section provides a brief discussion for each of the test sites.

4.1. *Aeolian landscape in Melas Chasma*

This terrain has been interpreted as composed of blowouts and pan marginal lunette dunes (Pardo-Igúzquiza and Dowd, 2022). This is a detached geomorphology in which sediments transported by the wind have covered the underlying bedrock. Curiously, the histogram of the local fractal of the aeolian landscape is almost identical to that of the

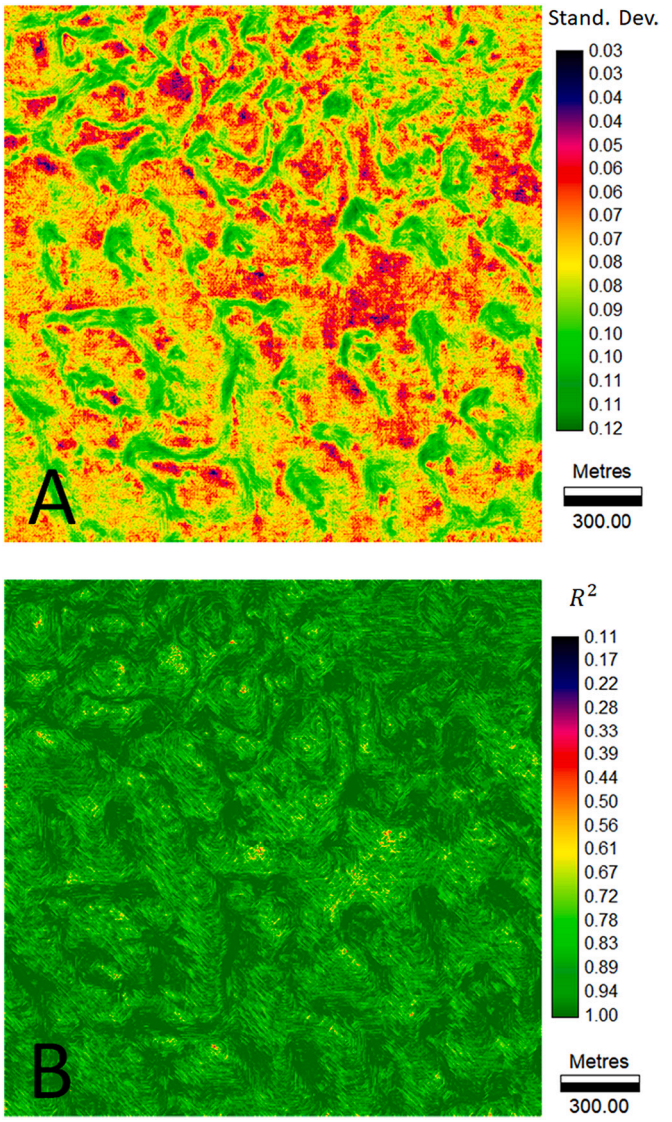

Fig. 10. A. Standard deviation of the estimated fractal dimension shown in Fig. 4A. B. Coefficient of determination (R^2) of the estimation of the fractal dimension shown in Fig. 4A.

cratered terrain. However, the spatial variability of the high and low values of roughness are in opposite topographic styles. In the aeolian terrain (Fig. 4B), the closed depressions (blowouts) correspond to areas with higher local fractal dimension (higher roughness) while the lunette dunes are areas of low roughness (low local fractal dimension). However, in the cratered terrain (Fig. 7B) the closed depressions (craters) are locations with lower roughness (low fractal dimensions). It is likely that in the blowout depressions the removal of the aeolian cover (deflation basin) has resurfaced an irregular bedrock while the aeolian dunes are relatively recent and are still smooth and not significantly affected by recent impact craters of small size. The variogram of local roughness for distances up to 200 m (Fig. 4C) reaches a plateau at around 120 m, which is the mean size of the main aeolian features in the image. Segmenting the roughness map in four quartiles, as described in Fig. 4D, shows the high connectivity or low fragmentation of the low values of roughness and their elongated shape.

4.2. Volcanic landscape in the northern part of Ulysses Tholus

This terrain has been interpreted as composed of erosion-transformed depressions and mounds (Pardo-Igúzquiza and Dowd, 2022). A volcanic terrain is formed by lava flows that have the topography of closed depressions and mounds that later will be smoothed by erosion processes. The histogram of the local fractal dimension of the volcanic terrain in Fig. 11A shows that this terrain has a little more roughness than the aeolian terrain previously considered. In the volcanic terrain the topographic mounts correspond to low roughness (low local topographic dimension) and the higher roughness is related to topographic depressions. A typical topographic profile of this terrain is given in Fig. 12B. The histograms of the volcanic terrains on Earth are given in Fig. 11B and these are much smoother than those in the Martian example. The variogram of local roughness for distances up to 200 m (Fig. 5C) reaches a plateau at around 70 m, which is the mean size of the main volcanic features in the image. At these short distances the spatial variability of roughness is isotropic. The segmentation of the roughness map into four quartiles, as described in Fig. 5D, shows more fragmentation of the low values of roughness than in the aeolian case and the volcanic features are more rounded than elongated in shape.

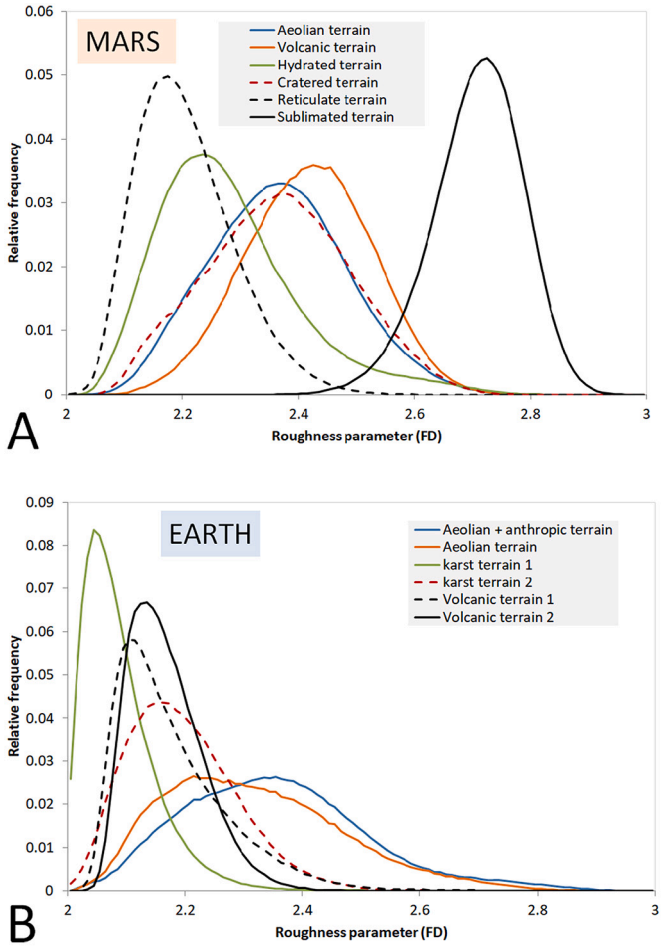

Fig. 11. Histogram of the roughness parameter (fractal dimension FD) for the six types of selected terrains.

4.3. Hydrated landscape inside Ius Chasma

This terrain has been interpreted as composed of an evaporite karst (Pardo-Igúzquiza and Dowd, 2022), similar to that of salt and gypsum diapirs on Earth (Hudec and Jackson, 2007) and similar to the diapirism found in the Hellas basin floor (Bernhardt et al., 2016). The local fractal dimension map is given in Fig. 6B and reveals spatial patterns that could be of significant interest in geomorphological and geological studies of this terrain. It has a flow type orientation (white arrow on the right-hand side of the image) and an area of very high roughness (white arrow on

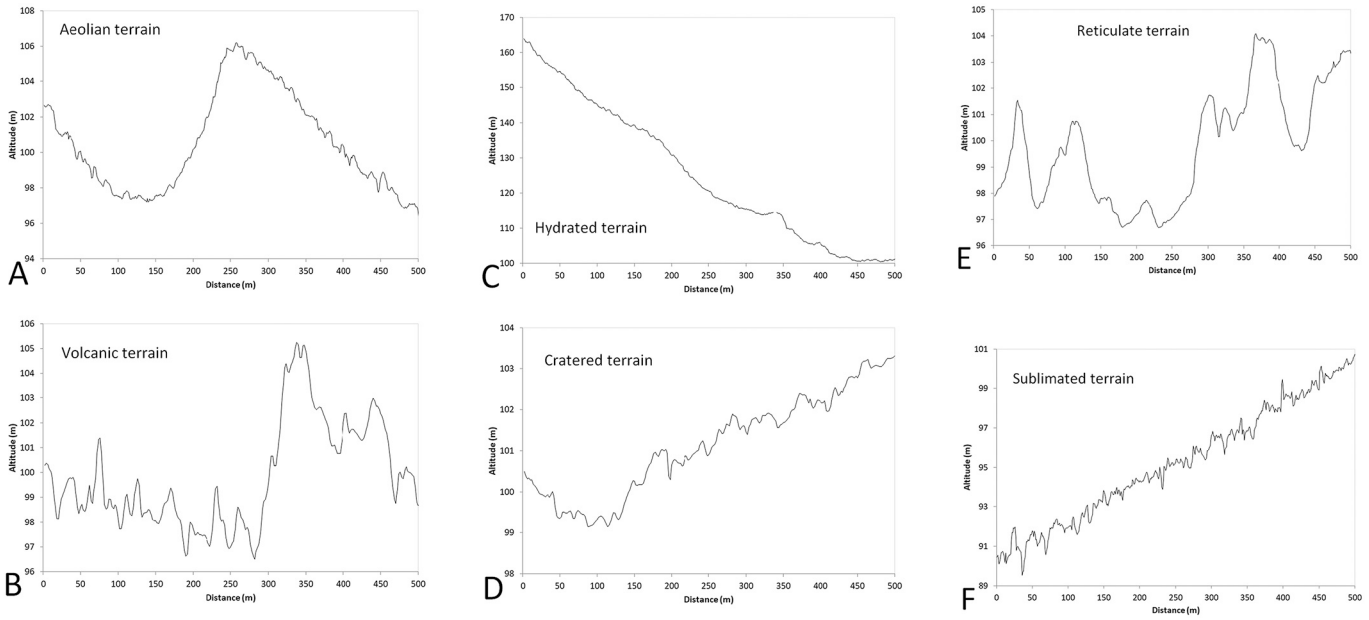

Fig. 12. Typical topographic profiles of half a kilometre length for the six terrain types and with roughness close to the means given in Table 1. A: 2.35; B: 2.42; C: 2.26; D: 2.37; E: 2.17 and F: 2.75.

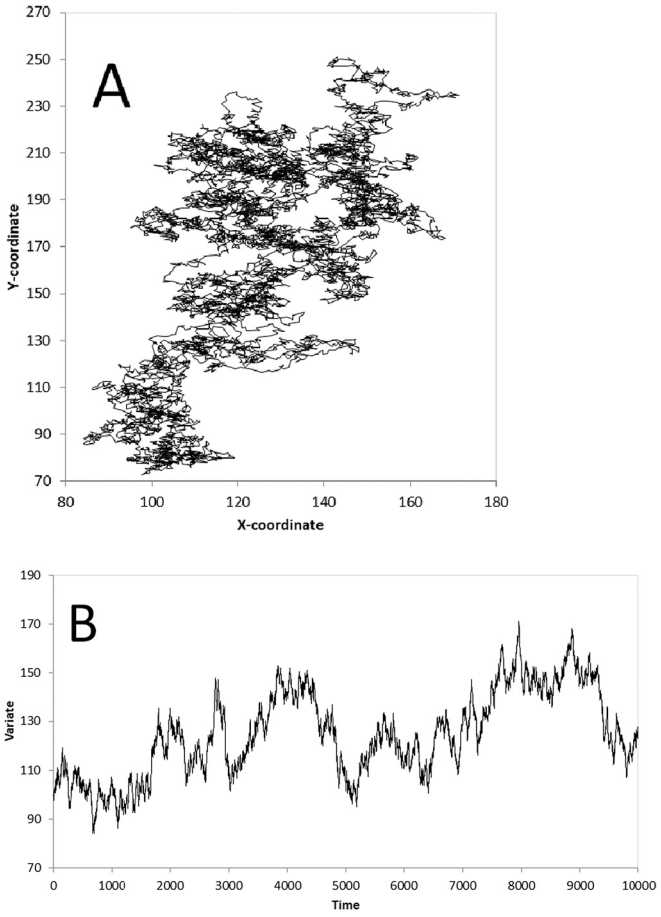

Fig. 13. One-dimensional random walk. A. Seen as a random walk on a plane. The random walk tends to fill the plane and has a Hausdorff dimension of 2. B. The random walk as a time series or topographic profile; with a HDF of 1.5.

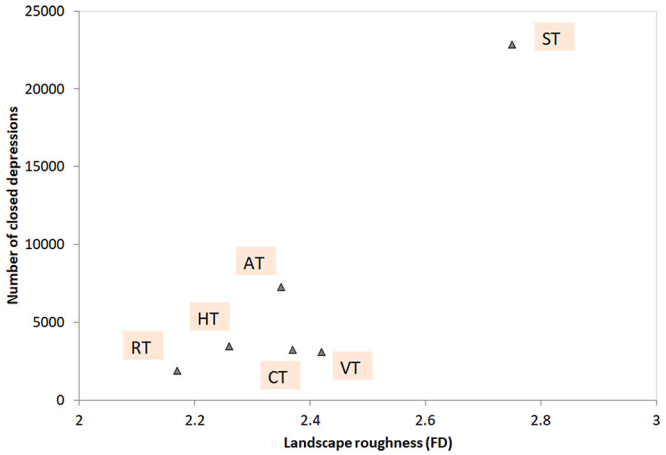

Fig. 14. Relationship between the landscape mean roughness of Martian topography and the number of closed terrain depressions in each test zone. AT: aeolian terrain; VT: volcanic terrain; CT: cratered terrain; HT: hydrated terrain; RT: reticulate terrain; ST: sublimated terrain.

the left-hand side of the image) even though the histogram of the local fractal dimension (Fig. 11A) shows that the terrain is quite smooth although it does have localised areas of high roughness. The plastic behaviour of the outcropping rocks in this terrain could explain the flow structures shown in the spatial variability of the local fractal dimension. The variogram of local roughness for distances up to 200 m (Fig. 6C) shows two breaks in the slope at 30 m and at 140 m where the variogram reaches a plateau. Thus, in this case, the spatial variability of roughness for short distances has small components of up to 30 m and larger components of up to 140 m that can be considered as the mean size of the geological features in the image. At these short distances the spatial variability of roughness is isotropic. The segmentation of the roughness map into four quartiles, as described in Fig. 6D, shows fragmentation similar to the volcanic case but with more elongated features.

4.4. Cratered landscape in the northern flank of Tharsis Tholus volcano

This terrain has been interpreted as a typical impact crater landscape (Pardo-Igúzquiza and Dowd, 2022). The local fractal dimension of this terrain has previously been compared with the aeolian terrain. The histograms of the local fractal dimension of both terrains are similar but the zones of low roughness correspond to impact craters (negative topographies) for this type of terrain while the same smooth surfaces were in the positive topographies (dunes) in the aeolian terrain. It seems that the impact craters have smoothed the terrain while the zones with ejected material around the craters correspond to the rough landscape in this type of terrain. The variogram of local roughness for distances up to 200 m (Fig. 7C) reaches a plateau at around 160 m, which is the mean size of the main volcanic features in the image. At these short distances the spatial variability of roughness is isotropic. The segmentation of the roughness map into four quartiles, as described in Fig. 7D, shows little fragmentation of the low values of roughness and their rounded shape.

4.5. Reticulate landscape in Lycus Sulci

This terrain has been interpreted as a jigsaw puzzle pattern of depressions and mounds (Pardo-Igúzquiza and Dowd, 2022) and a possible origin of this pattern could be the downslope movement of wall material caused by the viscous deformation of ground ice (Bridges et al., 2010). The histogram in Fig. 11A and the map of the local fractal dimension in Fig. 8B show that this terrain has the lowest values of local fractal dimension which implies smooth terrains or terrains with low roughness. This smoothness may be related to the small number of closed depressions as shown in the relationship in Fig. 14 and in the topographic profile in Fig. 12E. The variogram of local roughness for distances up to 200 m (Fig. 8C) reaches a plateau at around 30 m, which is the mean size of the geological features in the image. At these short distances the spatial variability of roughness is isotropic. The segmentation of the roughness map into four quartiles, as described in Fig. 7D, shows the high fragmentation of the low values of roughness, which is much larger than the aeolian, volcanic, hydrated and cratered terrains.

4.6. Sublimated landscape at the Southern pole

This terrain has been interpreted as negative and positive araneiforms (Hao et al., 2019; Pardo-Igúzquiza and Dowd, 2022) and the origin of this pattern is the seasonal sublimation of CO_2 (Schwamb et al., 2018). The histogram in Fig. 11A and the map of the local fractal dimension in Fig. 9B show that this terrain has the highest values of the local fractal dimension which implies a very rough terrain. This roughness appears to be related to the high number of small, closed depressions as shown in the relationship in Fig. 14 and in the topographic profile in Fig. 12F. The variogram of local roughness for distances up to 200 m (Fig. 8C) shows two breaks of slope at 5 m and at 30 m at which it reaches a plateau. Thus, the spatial variability of roughness shows that there are very small-scale geological features of mean size 5 m and 30 m. At these short distances the spatial variability of roughness is isotropic. The segmentation of the roughness map into four quartiles, as described in Fig. 8D, shows very high fragmentation of the low values of roughness, which are even larger than that of the reticulated terrain.

The roughness of Martian terrains and their spatial analysis provides another layer of information that can be integrated with other layers of information obtained from DEMs with different resolutions (Aharonson et al., 2001), HiRISE images (Keszthelyi et al., 2008), spectral imagery information generated by other sensors (Brown et al., 2012), etc. In this context, terrain roughness will provide useful information on Mars as applications on Earth have already done (Day and Chenoweth, 2013; Smith, 2014).

5. Conclusions

This paper presents the results of estimating surface roughness of local terrain tiles using the fractal dimension. The purpose of doing so is to quantify the terrain texture of different types of Martian terrain to provide roughness maps that will assist Planetary Geologists in understanding geological processes and formations. The novelty of the work is that the texture is characterized on a 1-m scale and maps of surface roughness have been generated for local zones of 2 km $\times$ 2 km, neither of which have been provided in any previous work. Six sites were selected as archetypes for major Martian terrain types: aeolian, volcanic, hydrated, cratered, reticulate and sublimated. The topography at these sites is represented by 1 to 2 m resolution DEMs constructed from stereopair HiRISE images. The moving window size of 41 $\times$ 41 cells are local tiles of the DEM for which a fractal dimension is calculated. The fractal dimension is obtained from 1D transects of the surface in principal directions by using the variogram. The fractal dimension assigned to a surface within a tile is an average of the four 1D fractal dimensions. The final result is a map showing the spatial distribution of local values of the fractal dimension across the site - a proxy for a map of local surface roughness on a 1-m scale. Following good statistical practice, uncertainty measures of the estimated roughness are provided.

The procedure does have its limitations. Landscape roughness is the result of many complex geological processes such as faulting, folding, erosion, deposition, mantling, resurfacing, mass movement, etc. It is thus unrealistic to expect that a map of surface roughness would be a diagnostic feature that unambiguously identifies a geological process or geological formation. Even on Earth that is not possible (Smith, 2014) and so it is even less likely to apply to Mars where our geological knowledge is still fragmentary and uncertain. However, and because of the latter, all tools and morphometric parameters that provide information on the local geology should be integrated in any geological or geomorphological study of Mars at the local scale. In this sense, the images of the topographic roughness of Mars at the metre-scale can be seen as a different view of the terrain that provides information on roughness variability and that can reveal hidden spatial structures that can assist in geomorphological and geological mapping and in the study of processes and products. It has been shown how, in general, the terrains on Martian landscapes are rougher than those on Earth because on Mars the impact cratering of small bodies creates roughness (like in the Moon as shown by Cai and Fa (2020)) while on Earth rainfall and sheet flow, together with the corresponding drainage network, will smooth the terrain. The sublimated terrain with its high roughness does not appear to have an equivalent on Earth. The images of local roughness presented in this paper, together with the method used to generate them, provide the planetary geologist with a means of extracting more useful information from the high-resolution digital elevation models from HiRISE images.

Data availability

All data and software used in this paper are freely available from the authors to anyone interested in reproducing the results or applying their own methods.

Declaration of Competing Interest

None.

Acknowledgements

The work of the first author was supported by research project PID2019-106435GB-I00 of the Ministerio de Ciencia e Innovación of Spain. The work of the second author was supported by the Australian Research Council Industrial Transformation Training Centre research project IC190100017. We thank the anonymous reviewers for their

constructive criticism that has helped to improve the final version of the paper.

References

Aharonson, O., Zuber, M.T., Neumann, G.A., Head III, J.W., 1998. Mars: Northern hemisphere slopes and slope distributions. Geophys. Res. Lett. 25 (24), 4413–4416.

Aharonson, O., Zuber, M.T., Rothman, D.H., 2001. Statistics of Mars' topography from Mars orbiter laser altimeter: slopes, correlations, and physical models. J. Geophys. Res. 106 (E10), 23723–23735.

Beran, J., 1994. Statistics for long-memory processes. In: Monographs on Statistics and Applied Probability, Vol. 61. Chapman & Hall, New York, 315 p.

Bernhardt, H., Reiss, D., Hiesinger, H., Ivanov, M.A., 2016. The honeycomb terrain on the Hellas basin floor, Mars: a case for salt or ice diapirism. J. Geophys. Res. Planets 121, 714–738.

Bridges, N.T., Banks, M.E., Beyer, R.A., Chuang, F.C., Noe Dobrea, E.Z., Herkenhoff, K.E., Keszthelyi, L.P., Fishbaugh, K.E., McEwan, A.S., Michaels, T.I., Thomson, B.J., Wray, J.J., 2010. Aeolian bedforms, yardangs, and indurated surfaces in the Tharsis Montes as seen by the HiRISE camera: evidence for dust aggregates. Icarus 205, 165–182.

Brown, A.J., Calvin, W.M., Murchie, S.L., 2012. Compact Reconnaissance Imaging Spectrometer for Mars(CRISM) north polar springtime recession mapping:First 3 Mars years of observations. J. Geophys. Res. 117, 1–19. E00J20.

Burrough, P.A., 1981. Fractal dimensions of landscapes and other environmental data. Nature 294, 240–242.

Cai, Y., Fa, W., 2020. Meter-scale topographic roughness of the moon: the effect of small impact craters. J. Geophys. Res. Planets 125 (8) e2020JE006429.

Cooper, M.A., Jordan, T.M., Schroeder, D.M., Siegert, M.J., Williams, C.N., Bamber, J.L., 2019. Subglacial roughness of the Greenland Ice Sheet: relationship with contemporary ice velocity and geology. Cryosphere 13, 3093–3115.

Day, M., Chenoweth, S., 2013. Surface roughness of karst landscapes. In: Shroder, J., Frumkin, A. (Eds.), Treatise on Geomorphology, Karst Geomorphology, Vol. 6. Academic Press, San Diego, CA, pp. 157–163.

De Vries, A.C., Kustas, W.P., Ritchie, J.C., Klaassen, W., Menenti, M., Rango, A., Prueger, J.H., 2003. Effective aerodynamic roughness estimated from airborne laser altimeter measurements if surface features. Int. J. Remote Sens. 24 (7), 1545–1558.

Deliège, A., Kleyntssens, T., Nicolay, 2017. Mars topography investigated through the wavelet leaders method: a multidimensional study of its fractal structure. Planet. Space Sci. 136, 46–58.

Draper, N.R., Smith, H., 1998. Applied Regression Analysis, Third edition. Wiley. 738 p.

Dubuc, B., Zucker, S.W., Tricot, C., Quiniou, J.F., Wehbi, D., 1989. Evaluating the fractal dimension of surfaces. Proc. R. Soc. Lond. A Math. Phys. Sci. 425, 113–127.

Fox, C.G., Hayes, D.E., 1985. Quantitative methods for analysing the roughness of the seafloor. Rev. Geophys. 23 (1), 1–48.

Franceschetti, G., Iodice, A., Migliaccio, M., Riccio, D., 1999. Scattering from natural rough surfaces modeled by fractional Brownian motion two-dimensional processes. IEEE Trans. Antennas Propag. 47, 1405–1415.

Garneau, S., Plaut, J.J., 2000. Topographic and roughness characteristics of the Vastitas Borealis formation on Mars described by fractal statistics. In: Lunar and Planetary Science XXXI abstract 1115, 2 p.

Gerekos, C., Grima, C., Steinbrügge, G., Thakur, S., Scanlan, K.M., Young, D.A., Bruzzone, L., Blankenship, D.D., 2021. Martian roughness analogues of European terrains for radar sounder investigations. Icarus 358, 114197.

Gilbert, L.E., 1989. Are topographic data sets fractal? In: Scholz, C.H., Mandelbrot, B.B. (Eds.), Fractals in Geophysics. Pure and Applied Geophysics, Birkhäuser, Basel.

Glenn, N.F., Thackray, G.D., Dorsch, S.J., Streutker, D.R., Chadwick, D.J., 2006. Analysis of LiDAR-derived topographic information for characterizing and differentiating landslide morphology and activity. Geomorphology 73, 131–148.

Gneiting, T., Schlather, M., 2004. Stochastic models that separate fractal dimension and the Hurst effect. SIAM Rev. 46, 269–282.

Gneiting, T., Ševčíková, H., Percival, D.B., 2012. Estimators of fractal dimension: assessing the roughness of time series and spatial data. Stat. Sci. 27, 247–277.

Graf, J.E., Zurek, R.W., Eisen, H.J., Jai, B., Johnston, M.D., DePaula, R., 2005. The Mars reconnaissance orbiter Mission. Acta Astronaut. 57 (2–8), 566–578.

Grohmann, C.H., Smith, M.J., Riccomini, C., 2011. Multi-scale analysis of topographic surface roughness in the Midland Valley, Scotland. IEEE Trans. Geosci. Remote Sens. 49, 1200–1213.

Hao, J., Michael, G.G., Adeli, S., Jaumann, R., 2019. Araneiform terrain formation in Angustus Labyrinthus, Mars. Icarus 317, 479–490.

Hayes, D.E., Kane, K.A., 1991. The dependence of seafloor roughness on spreading rate. Geophys. Res. Lett. 18 (8), 1425–1428.

Huang, J., Turcotte, D.L., 1989. Fractal mapping of digitized images: application to the topography of Arizona and comparisons with synthetic images. J. Geophys. Res. Solid Earth 94 (B6), 7491–7495.

Hudec, M.R., Jackson, M.P.A., 2007. Terra infirma: understanding salt tectonics. Earth Sci. Rev. 82, 1–28.

Journel, A.G., Huijbregts, Ch.J., 1978. Mining Geostatistics. Academic Press, New York, p. 600.

Keszthelyi, L., Jaeger, W., McEwen, A., Tornabene, L., Beyer, R.A., Dundas, C., Milazzo, M., 2008. High resolution imaging science experiment (HiRISE) images of volcanic terrains from the first 6 months of the Mars reconnaissance orbiter primary science phase. J. Geophys. Res. Planets 113 (E04005), 1–25.

Kim, J.-R., Lin, S.-Y., Muller, J.-P., Warner, N.H., Gupta, S., 2013. Multi-resolution digital terrain models and their potential for Mars landing site assessments. Planet. Space Sci. 85, 89–105.

Klinkenberg, B., 1992. Fractals and morphometric measures: is there a relationship? In: Snow, R.S., Mayer, L. (Eds.), Fractals in Geomorphology, Geomorphology, Vol. 5, pp. 5–20.

Krelavsky, M.A., Head, J.W., 2000. Kilometer-scale roughness of Mars: results from MOLA data analysis. J. Geophys. Res. 105, 26695–26712.

Liu, Y., Yang, Y., Chen, K.-S., 2021. Martian topographic roughness spectra and its influence on Bistatic radar scattering. IEEE Geosci. Remote Sens. 18 (11), 1951–1955.

Mandelbrot, B., 1977. Fractals, Form, Chance and Dimension Freeman, San Francisco.

Mandelbrot, B., 1983. The Fractal Geometry of Nature. Freeman, San Francisco, 460 pp.

Marston, B.E., Jenny, B., 2015. Improving the representation of major landforms in analytical relief shading. Int. J. Geogr. Inf. Sci. 29 (7), 1–22.

Martano, P., 2000. Estimation of surface roughness length and displacement height from single-level sonic anemometer data. J. Appl. Meteorol. 39, 708–715.

Matheron, G., 1963. Principles of geostatistics. Econ. Geol. 58, 1246–1266.

McEwen, A.S., Banks, M.E., Baugh, N., Becker, K., Boyd, A., Bergstrom, J.W., Beyer, R.A., Bortolini, E., Bridges, N.T., Byrne, S., et al., 2010. The high resolution imaging science experiment (HiRISE) during MRO's primary science phase (PSP). Icarus 205 (81), 2–37.

Orosei, R., Bianchi, R., Coradini, A., Espinasse, S., Federico, C., Ferriccioni, A., Gavrishin, A.I., 2003. Self-affine behaviour of Martian topography at kilometer scale from Mars orbiter laser altimeter data. J. Geophys. Res. 108 (E4), 1–10, 8023.

Pardo-Igúzquiza, E., 1997. GCINFE: a computer program for the inference of polynomial generalized covariance functions. Comput. Geosci. 23 (2), 163–174.

Pardo-Igúzquiza, E., 1998. MLREML4: a program for the inference of the power variogram model by maximum likelihood and restricted maximum likelihood. Comput. Geosci. 24 (6), 537–543.

Pardo-Igúzquiza, E., Dowd, P.A., 2003. IRFK2D: a computer program for simulating intrinsic random functions of order k. Comput. Geosci. 29, 753–759.

Pardo-Igúzquiza, E., Dowd, P.A., 2020. Fractal analysis of karst landscapes. Math. Geosci. 52, 543–563.

Pardo-Igúzquiza, E., Dowd, P.A., 2022. Fractal analysis of the Martian landscape: a study of kilometre-scale topographic roughness. Icarus 372, 114727. https://doi.org/10.1016/j.icarus.2021.114727.

Riley, S.J., DeGloria, S.D., Elliot, R., 1999. A terrain ruggedness index that quantifies topographic heterogeneity. Intermount. J. Sci. 5 (1–4), 23–27.

Robbins, S.J., 2018. The fractal nature of planetary landforms and implications to geological mapping. Earth Space Sci. 5, 211–220.

Schwamb, M.E., Aye, K.M., Portyankina, G., Hansen, C.J., Allen, C., Allen, S., Calef, F.J., Duca, S., McMaster, Miller, G.R.M., 2018. Planet four: terrains – discovery of araneiforms outside of the south polar layered deposits. Icarus 308, 148–187.

Schwimmer, R.A., 2008. A temporal geometric analysis of eroding marsh shorelines: can fractal dimensions be related to process? J. Coast. Res. 24 (1), 152–158.

Segal, R.A., Scharien, R.K., Cafarella, S., Tedstone, A., 2020. Characterizing winter landfast sea-ice surface roughness in the Canadian Arctic archipelago using Sentinel-1 synthetic aperture radar and the multi-angle imaging SpectroRadiometer. Ann. Glaciol. 61 (83), 284–298.

Sharma, P., Byrne, S., 2010. Constraints on Titan's topography through fractal analysis of shorelines. Icarus 209, 723–737.

Shepard, M.K., Campbell, B.A., 1999. Radar scattering from a self-affine fractal surface: near-nadir regime. Icarus 141 (1), 156–171.

Shepard, M.K., Campbell, B.A., Bulmer, M.H., Farr, T.G., Gaddis, L.R., Plaut, J.J., 2001. The roughness of natural terrain: a planetary and remote sensing perspective. J. Geophys. Res. 106 (E12), 32777–32795.

Smith, M.W., 2014. Roughness in the earth sciences. Earth Sci. Rev. 136, 202–225.

Smith, D.E., Zuber, M.T., Frey, H.V., Garvin, J.B., Head, J.W., Muhleman, D.O., Pettengill, G.H., Phillips, R.J., Solomon, S.C., Zwally, H.J., Banerdt, W.B., Duxbury, T.C., Golombek, M.P., Lemoine, F.G., Neumann, G.A., Rowlands, D.D., Aharonson, O., Ford, P.G., Ivanov, A.B., Johnson, C.L., McGovern, P.J., Abshire, J.B., Afzal, R.S., Sun, X., 2001. Mars orbiter laser altimeter: experiment summary after the first year of global mapping of Mars. J. Geophys. Res. 106, 23689–23722.

Taud, H., Parrot, J.-F., 2005. Measurement of DEM roughness using the local fractal dimension. Géomorphol. Relief Processus Environ. 11, 327–338.

Volker, H.X., Wasklewicz, T.A., Ellis, M.A., 2007. A topographic fingerprint to distinguish alluvial fan formative processes. Geomorphology 88, 34–45.

Voss, R.F., 1985. Random fractal forgeries. In: Earnshaw, R.A. (Ed.), Fundamental Algorithms for Computer Graphics: NATO ASI Series, Vol. 17. Springer, Berlin, pp. 805–835.

Wen, R., Sinding-Larsen, R., 1997. Uncertainty in fractal dimension estimated from the power spectra and variograms. Math. Geol. 29, 727–753.

Wilson, M.F.J., O'Connell, B., Brown, C., Guinan, J.C., Grehan, A.J., 2007. Multiscale terrain analysis of multibeam bathymetry data for habitat mapping on the continental slope. Mar. Geod. 30 (1–2), 3–35.

Xu, T., Moore, I.D., Gallant, J.C., 1993. Fractals, fractal dimensions and landscapes – a review. Geomorphology 8, 245–262.